Journal of Optoelectronic and Biomedical Materials Vol. 18, No. 2, April–June 2026, p. 16-43

Original Research

Growth, Structural Characterization, and NLO Behavior of Picolinic Acid Copper Sulfate Crystals: A Dual-Functional Material for Optical and Antibacterial Applications

Raja Mohan O S [1], M. S. Malar Selvi [2], R. Rathika [3], J. Subashini [4], T. U. Jeevitha [1,5], Senthil S [1,*]

[1] Department of Physics, Chennai Institute of Technology, Chennai-600069, Tamilnadu, India.
[2] Department of Chemistry, Chennai Institute of Technology, Chennai-600069, Tamilnadu, India.
[3] PG and Research Department of Physics, Thanthai Hans Rover College (Autonomous), Perambalur – 621 220, Tamilnadu, India.
[4] Department of Physics, Bharath Institute of Science & Technology, Bharath Institute of Higher Education and Research, Chennai-600073, Tamilnadu, India.
[5] Department of Physics, Academy of Maritime Education and Training, Chennai, Tamil Nadu 603112, India.
* Correspondence: ssenthil_14@yahoo.co.in

Received: January 2, 2026; Accepted: April 14, 2026

Abstract: Picolinic acid copper sulfate (PACS) crystals have been prepared by slow evaporation method and their structural characteristics, optical characteristics, nonlinear optical (NLO) characteristics, as well as antibacterial characteristics are systematically examined. X-ray diffraction analysis in the form of powder revealed the crystalline structure of PACS that is monoclinic in nature and possesses good phase purity. The existence of typical functional groups and metal-ligands interactions within the crystal lattice were confirmed using Raman and FTIR spectroscopy. The optical investigation by the UV-Vis spectroscopy has shown that the band gap is about 1.8 eV which means the material is transparent in the visible spectrum and it can be used in the field of optoelectronics. The field-emission scanning electron microscopy revealed a homogenous crystal morphology with properly developed surfaces. The Z-scan method was used to measure nonlinear optical properties, and the results obtained indicate that the nonlinear refractive index of the material was $n_2 = 3.51 \times 10^{-10}$ cm^2/W, the nonlinear absorption coefficient was $b = 3.81 \times 10^{-6}$ cm/W, and the third-order susceptibility was $\chi^{(3)} = 4.77 \times 10^{-8}$ esu, which is a good indicator of strong NLO activity. Antibacterial tests on Staphylococcus aureus, Staphylococcus epidermidis and Escherichia coli showed high zones of inhibition which showed potential promising antimicrobial activity. The optical and antibacterial dual functionality indicates that PACS crystals could be considered as multifunctional in the applications in photonic equipment, optical limiters and antimicrobial coating.

Keywords: PACS crystals; nonlinear optical materials; third-order susceptibility; UV photonic applications; antibacterial activity; multifunctional materials; Z-scan analysis.

---

1. Introduction

Semi-organic crystals are gaining popularity in advanced materials research due to their unique features, which combine the high optical nonlinearity and processability of organic molecules with the mechanical strength and thermal stability of inorganic salts [1-4]. In particular, the synthesis of crystals that combine nonlinear optical (NLO) activity with antibacterial functionality is a burgeoning yet underexplored field. Although numerous materials are recognized for their distinctive optical or biological properties, only a limited number have been systematically investigated for dual-functionality within a single crystalline system, particularly under conditions suitable for practical applications in biomedicine and photonics.

Picolinic acid, a pyridine-based bidentate ligand, has both a nitrogen atom in its aromatic ring and a carboxylic acid group, allowing for strong metal-ligand interactions that are extremely favorable for charge-transfer mechanisms—a critical prerequisite for improved NLO performance [5]. Furthermore, picolinic acid and its derivatives are known for a wide spectrum of biological activities, including antibacterial, anticancer, and anti-inflammatory properties, making them promising candidates for medicinal material development [6-8].

The addition of copper ions (Cu^{2+}) into such molecular structures has added functional benefits. Compounds based on copper have received significant research attention due to their versatile coordination chemistry, tunable electronic structure and their extensive application in catalysis, photonics, sensing and biomedical systems. In the recent past, the importance of copper complexes in optical, catalytic, and antimicrobial applications has been emphasized because of their property to mediate electron transfer and redox reactions [9-10]. Additionally, copper coordination compounds have also shown a striking structural versatility and multifunctional capability in inorganic and hybrid materials [11-13]. In particular, copper compounds are well known for their photoluminescent behavior, catalytic activity, and antibacterial efficacy, which originates from their ability to disrupt bacterial membranes and interfere with enzymatic processes through redox cycling and ion exchange mechanisms [14-17]. Additionally, copper-based materials possess electron transport properties that are advantageous in photonic applications, rendering them suitable for optical-electronic integration [18-19]. However, the nonlinear optical characteristics and general bioactivity of picolinic acid–copper sulfate complexes in crystalline form remain largely unexplored.

To the best of our knowledge, this is the first systematic investigation of picolinic acid copper sulfate (PACS) crystals combining nonlinear optical (NLO) response with antibacterial functionality within a single semi-organic crystalline system. The present study not only reports the successful growth of PACS crystals but also establishes a correlation between their structural features, optical properties, and biological activity through comprehensive characterization techniques.

To address this scientific gap, we provide a unique synthesis and comprehensive characterisation of Picolinic Acid Copper Sulfate (PACS) crystal grown by the slow evaporation technique, a semi-organic crystal tailored to have both significant NLO activity and antibacterial properties. A broad set of characterisation approaches is used in our approach to emphasize structure-property relationships. Powder X-ray Diffraction (XRD) was employed to assess phase purity and lattice parameters, whereas Fourier Transform Infrared Spectroscopy (FT-IR) confirmed molecular interactions and ligand coordination [20]. UV-Visible-Near Infrared (UV-Vis-NIR) spectroscopy revealed an optical band gap that promotes photonic transparency, implying that PACS is suitable for optoelectronic and optical limiting applications [21]. Microhardness testing was used to determine the mechanical durability of the crystals [22], while etching experiments revealed crystal formation mechanisms and defect patterns [23].

Second Harmonic Generation (SHG) experiments showed the presence of high NLO activity in PACS crystals [24], demonstrating their suitability for application in frequency-doubling devices and optical modulators. In parallel, antibacterial assays against both Gram-positive and Gram-negative bacterial strains revealed significant inhibition zones, highlighting PACS crystals' efficacy in biomedical and environmental applications such as antimicrobial coatings and water purification membranes [25].

PACS stands out from other materials studied in the literature due to its combined optical and antibacterial functionality within a single semi-organic crystalline system. The material exhibits measurable SHG efficiency along with antibacterial activity, indicating its potential use in multifunctional platforms for photonic and biomedical technology. These chemicals have applications in bio-optical diagnostics, photonic sensors, medical device coatings, and multifunctional hybrid systems that respond rapidly to biological and optical stimuli.

Although these features definitely appeal to some extent, there are certain things that should be mentioned. In this study, the structural analysis is mainly based on the method of powder X-ray diffraction instead of refinements based on single-crystal X-ray diffraction, and therefore the bonding environments and atomic positions cannot be determined accurately. Moreover, additional investigations based on high-level structural analysis, long-term stability analysis, and device-level analysis performance must be urgently conducted that will help to fully elucidate the structure-property relations and the technological importance of PACS crystals. These considerations give a lot of guidance to the upcoming research projects.

This work provides one of the first systematic studies on picolinic acid-copper sulfate based semi-organic crystals, focusing on their optical and antibacterial properties. The results contribute to the growing field of multifunctional bio-photonic materials and may stimulate further research toward optoelectronics, environmental engineering, and biomedicine application.

2. Experimental methods

This work used high-purity reagents and solvents to ensure the efficient synthesis and crystallization of Picolinic Acid Copper Sulphate (PACS) crystals. All chemicals employed were of Analytical Reagent (AR) grade, guaranteeing minimal impurities and optimal reaction conditions. PACS was synthesized with 99% pure picolinic acid ($C_6H_5NO_2$) from Merck and 99.9% pure copper(II) sulfate ($CuSO_4$). The PACS crystals were synthesized by combining picolinic acid with copper sulfate in a 1:1 molar ratio. The chemical equation below delineates the procedure for synthesizing the complex.

$$C_6H_5NO_2 + CuSO_4 \rightarrow C_6H_5NO_2CuSO_4 \tag{1}$$

Initially, the quantity of picolinic acid was dissolved in deionized water while the stirring rate was maintained. The dissolving method took approximately three hours to achieve complete solubility and homogenous dispersion of the acid molecules. Aqueous copper(II) sulfate solution was then slowly added to the picolinic acid solution while stirring constantly. The addition was done gradually to reduce local supersaturation and precipitation, resulting in a clear, homogeneous solution. After mixing and homogenizing the solution, the reaction mixture was allowed to cool to room temperature. The translucent solution was purified using Whatman No. 1 filter paper to remove any undissolved particles or impurities. The filtrate was carefully transferred to a clean, dry beaker to avoid contamination during crystallization.

The slow evaporation approach was used to crystallize the material at ambient temperature in a contamination-free environment. Over time, characteristic PACS crystals began to nucleate and grow from the supersaturated solution. The growth phase was regularly monitored until large, optically clear crystals suitable for characterization were obtained. Figure 1 depicts the PACS single crystals formed from the growing medium. The crystals exhibit exceptional clarity, distinct facets, and an appropriate size for future physical, optical, and biological characterization research.

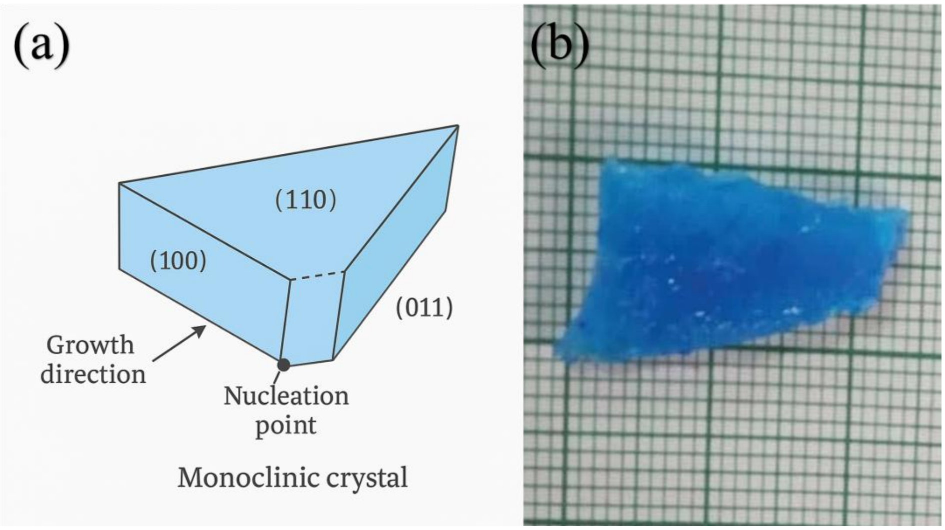

Figure 1. Photograph of as-grown PACS single crystal.

3. Result and discussion

3.1. X-ray diffraction (XRD) analysis of picolinic acid copper sulphate (PACS)

The synthesis of the Picolinic Acid Copper Sulphate (PACS) crystals ($C_6H_5NO_2{*}CuSO_4$) was conducted through the slow evaporation solution growth. Powder X-ray diffraction (PXRD) was used to investigate the crystalline nature and phase formation of the material obtained and the results were provided in Table 1 and Figure 2. The PXRD pattern was measured in Bruker Kappa APEXII X-ray diffractometer that showed a number of sharp and well-dispersed diffraction peaks which indicated the high crystallinity and purity of phases of the synthesized PACS compound.

Diffraction pattern may be indexed using a monoclinic crystal system with space group P21/c (tentatively) which is in agreement with structurally related copper-picolinate compounds that have been described in the literature [26]. The lack of any further impurity peaks means that the synthesized product is single phase inside the detection limits of PXRD implying the successful synthesis of the PACS compound in a good structural state.

The estimated lattice parameters of the indexed diffraction peaks were a = 10.1 **Å**, b = 7.8 **Å** and c = 13.2 **Å** with an approximate calculated unit cell volume of about 1023 **Å³** which validated the monoclinic structure framework of the material. The crystallite size of the sample determined by the Scherrer equation was 9.15 nm on average, which proved the presence of nanocrystalline PACS in the sample. Moreover, the Williamson-Hall (W-H) analysis was used to measure the lattice strain and the results showed that the micro strain was around 0.0046 indicating a comparatively small lattice deformation and excellent structural stability.

Close observation of the PXRD pattern shows that the study had diffraction peaks at 2 θ = 12.68°, 15.05°, 17.89°, 19.62°, 20.49°, 23.33°, 24.74°, 25.66°, 26.35°, 27.76°, and 35.17° indexed to the respective crystallographic planes **(100), (011), (110), (111), (200), (201), (102), (202), (120), (211), and (221)**, These observations affirm the crystallographic arrangement that was well defined with the monoclinic structure [27]. The derived crystallite sizes of these peaks were determined to be in the nanometer range thus supporting again the nanocrystalline nature of the PACS material.

All in all, the PXRD results indicate that the slow evaporation growth method was effective in obtaining high levels of crystalline PACS material with a clearly defined monoclinic structure. The purity of the phase, sharp diffraction, and the stability of the lattice parameters point to the fact that the synthesized PACS compound has a high quality structure and can be used in the further research of its optical, electrical, and functional characteristics, especially in the field of optoelectronics and sensors.

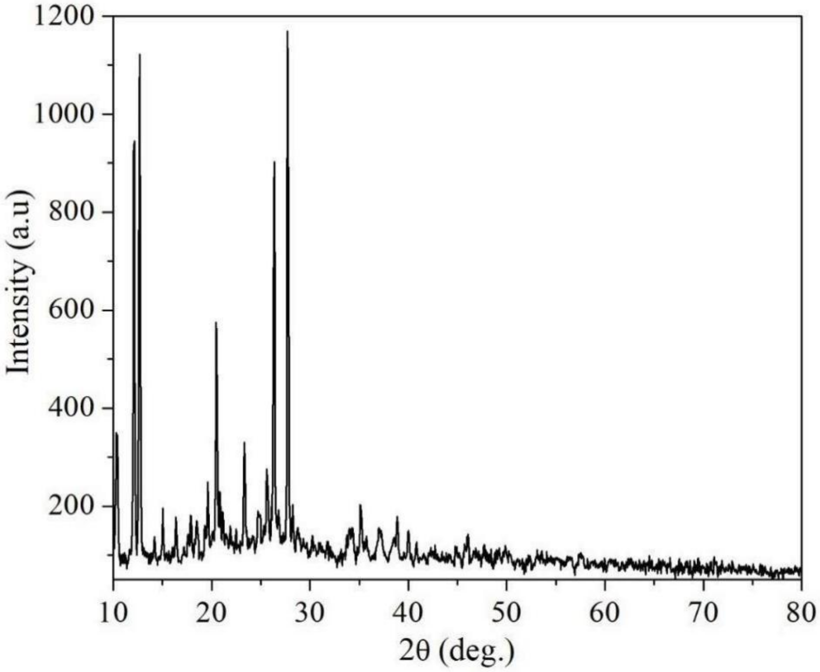

Figure 2. X-ray powder diffraction pattern for PACS crystals.

Table 1. Single-crystal XRD parameters of PACS crystal.

Parameter	Value
Chemical Formula	$C_6H_5NO_2{\cdot}CuSO_4$
Crystal System	Monoclinic (indexed)
Space Group	$P2_1/c$ (tentative)
Lattice Parameter a (Å)	10.1
Lattice Parameter b (Å)	7.8
Lattice Parameter c (Å)	13.2
Unit Cell Volume (Å^3)	1023
Phase Purity	Single phase
Major Miller Indices (hkl)	(100), (011), (110), (111), (200)
ICDD/JCPDS	Not available
COD Reference	7008235 (related copper–picolinate structure)

Table 2. Characteristics of XRD data obtained for PACS crystals.

Position (2θ)	d-Spacing	FWHM	Crystal Size (D) (nm)	Major Miller Indices (hkl)
12.6808	6.98058	0.1968	7.09	(100)
15.0579	5.88378	0.1476	9.48	(011)
17.8901	4.95821	0.1476	9.51	(110)
19.6205	4.52466	0.0984	14.30	(111)
20.4924	4.33368	0.1476	9.55	(200)
23.3297	3.813	0.1476	9.59	(201)
24.7428	3.59834	0.2952	4.81	(102)
25.6567	3.4722	0.1476	9.63	(202)
26.3465	3.38285	0.1476	9.65	(120)
27.757	3.21406	0.1476	9.68	(211)
35.17	2.55156	0.1968	7.39	(221)
Average Crystallite Size			9.15nm	

3.2. Fourier transform infrared spectroscopy (FTIR)

Fourier Transform Infrared (FTIR) spectroscopy was utilized to elucidate the functional groups and verify the molecular coordination in the freshly synthesized PACS (Picolinic Acid Copper Sulphate) crystals. Figure 3 depicts the FTIR spectrum obtained in the 400–4000 cm^{-1} range using the KBr pellet technique on a PERKIN ELMER FTIR spectrometer.

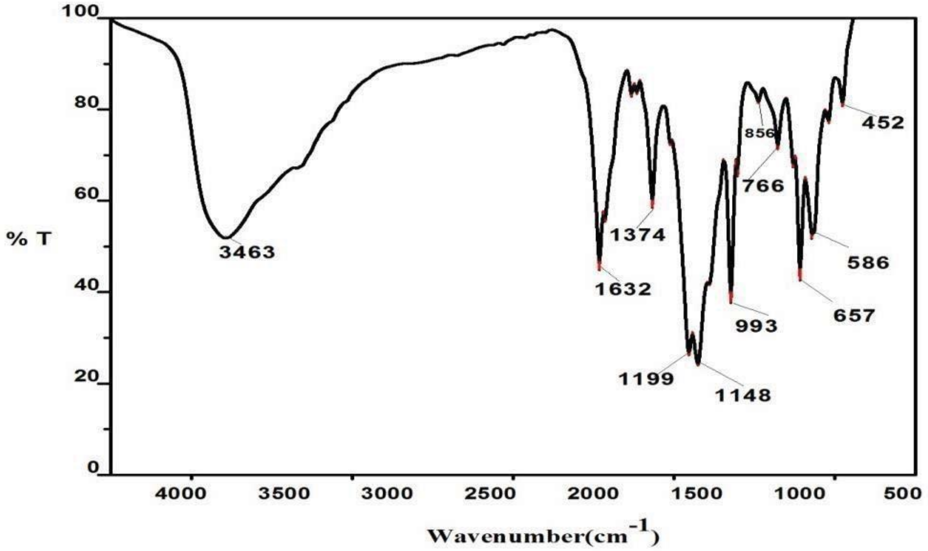

Figure 3. FTIR Spectrum of PACS single crystal.

This spectral analysis provides valuable insights into the molecular bonding environment and ligand–metal interactions within the PACS crystal lattice, thereby illustrating coordination-induced structural stabilization between aromatic carboxylate ligands and Cu^{2+} centers (Table 3) [28].

The general absorption band at 3463 cm^{-1} is explained as O-H vibration of hydrogen-bonded hydroxyl groups, which are most commonly produced by lattice entrapped or coordinated water molecules. The fact that crystallization water is in the coordination network is also evidenced by the presence of the strong band at 1632 cm^{-1}, which is attributed to H-O-H bending vibrations [29-30]. The relative strength of such bands implies that the hydrogen-bonding of interactions within the crystal structure of PACS occurs, which helps to stabilize the lattice (Table 4).

The spectral characteristics at 1374 cm^{-1}, 1199 cm^{-1} and 1148cm^{-1} are attributed to asymmetric C=O and aromatic C-N/C-C skeletal vibrations that proves the presence of picolinic acid ligands to coordinate with the metal center. Other peaks that could be seen at 993 cm^{-1} and 856 cm^{-1} are C-O stretching and ligand-related vibrations, and this suggests the formation of a coordinated metal-organic structure in the PACS lattice.

The appearance of strong bands in the low-wavenumber region (766, 657, 586, and 452 cm^{-1}) is caused by the lattice vibrations of copper-oxygen (Cu-O), which means that the copper ions, as well as the oxygen atom of the coordinating ligands, interact with each other. These vibrational modes give evidence of the formation of metal-ligand complexes in the semi-organic crystal structure.

The former section on Cu-O bond lengths, force constants and bonding strength based on FTIR spectra has been deleted in the updated manuscript because these parameters are not measurable using FTIR analysis alone, without crystallographic refinement or theory. Rather, the FTIR results are discussed qualitatively to verify the existence of the metal-ligand coordination and functional group in the PACS structure.

More so, no other peaks with usual impurities like carbonate, nitrate or other auxiliary forms are found, which means that the synthesized PACS crystals are highly pure in terms of chemicals and structurally homogeneous. On the whole, the FTIR analysis proves that the coordination between picolinic acid ligands and copper ions is effective, and it is possible to consider the formation of a stable semi-organic PACS crystalline skeleton. Such structural characteristics bring about the functional stability of the material that will be significant in the possible application in optoelectronic and bio-functional materials.

Table 3. FTIR peak assignment and functional group analysis.

Sample	Wavenumber (cm^{-1})	Transmittance (%)	Functional Group	Crystallinity Index (%)	Interpretation
PACS	3463	~40%	O–H stretching (H-bonded)	Moderate	Indicates moisture or –OH from acid group
PACS	1632	~60%	C=O stretching (carboxyl)	High	Confirms carboxylate ligand
PACS	1374	~70%	C–N or CH_3 bending	Good	Supports aromatic amine group
PACS	1199, 1148	~65–75%	C–O stretching	Good	Indicative of ester or ether group
PACS	993	~75%	C–H bending (aromatic)	High	Aromatic ring vibrations
PACS	766, 856	~70%	M–O (Cu–O or	High	Metal-ligand coordination

			SO_4^{2-}) bending		
PACS	657, 586, 452	~80%	Cu–O lattice vibrations	Strong	Confirms Cu–O bonding in the framework

Table 4. Derived parameters from FTIR spectrum.

Parameter	Value	Observation
Metal–Oxygen Bond Vibrations (cm^{-1})	452, 586, 657	Indicates Cu–O lattice vibrations, confirms metal-ligand coordination
Functional Group Identified	–OH, C=O, C–N, C–O, M–O	Confirmed through characteristic FTIR peaks
Band Intensity & Absorbance Ratio	3463 vs. 1632 cm^{-1}	Strong OH and C=O peaks suggest presence of hydrogen bonding
Chemical Stability	stable	No additional impurity peaks detected in the FTIR spectrum
Presence of Secondary Phase	None detected	Absence of extra peaks confirms phase purity

3.3. Optical transparency and electronic structure investigation through UV–Vis–NIR analysis

Using a Perkin Elmer Lambda 35 UV–Vis–NIR spectrophotometer, a thorough UV–Vis–NIR spectral analysis was performed to explore the optoelectronic potential and define the nonlinear optical (NLO) properties of the synthesized PACS (Picolinic Acid Copper Sulphate) crystal over a broad spectral range of 190–1100 nm. This analysis proves essential to determining transparency, absorption kinetics, and optical band structure—parameters crucial for the design and integration of next-generation photonic and optoelectronic mechanisms. Figure 4 shows the acknowledged transmission characteristics of the PACS.

Table 5. Optical parameters derived from UV–visible spectroscopy.

Parameter	Value	Observation
Wavelength Range Analyzed	200–1200 nm	Covers UV to near-infrared region
Transmission Range	0% – 95%	Indicates strong optical transparency above 400 nm
Absorption Edge (λ_{cutoff})	~680 nm	The onset of strong absorption corresponds to the band gap
Optical Band Gap (Eg)	1.8 eV	Direct allowed transition (from Tauc plot)
Urbach Energy (E_U)	~200 meV	Suggests the presence of localized states/disorder near the band edge
Nature of Transition	Direct Allowed	Confirmed from the linear Tauc plot $(\alpha h\nu)^2$ vs. $h\nu$
Refractive Index (n)	~2.3	Estimated using the empirical Moss relation ($n^2Eg \approx$ constant)
Extinction Coefficient (k)	~0.54	Indicates measurable absorption in UV region
Dielectric Constant (ε_r)	≈ 5.3	Estimated from (ε_r)using Penn's model
Absorption Coefficient (α)	10^4–10^5 cm^{-1}	High absorption in the UV region
Transparency	High	Supports use in optical devices; excellent light transmittance
Band Tail States	Present	Evident from the exponential Urbach tail
Chemical Stability	Stable	No photodegradation observed during UV exposure

Optical Quality	Good	Sharp band edge and high transmittance make it suitable for optoelectronic use

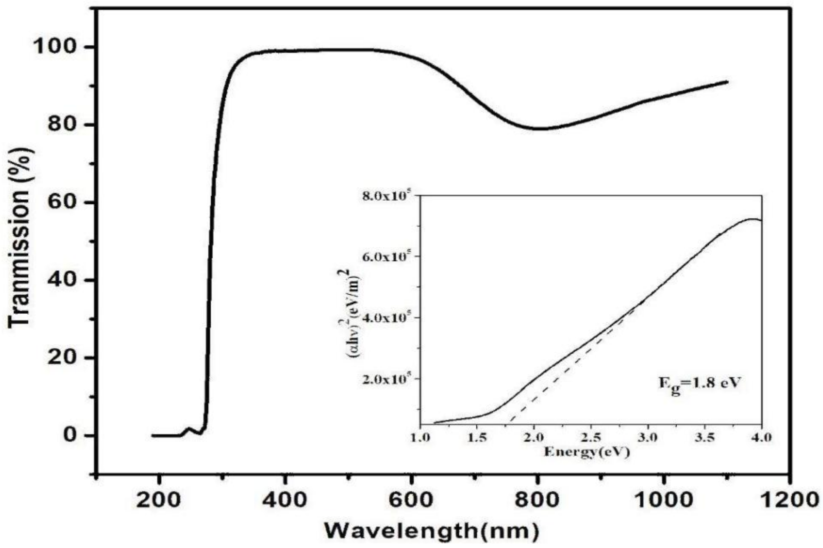

Figure 4. UV-vis-NIR spectrum of PACS single crystal.

The optical transmission spectrum has a distinctive absorption edge at 281 nm, signifying few imperfections and a well-structured crystalline lattice. Beyond the cut-off wavelength, the PACS crystal has remarkable transmittance exceeding 91% at 1100 nm, indicating little intrinsic optical loss over the visible to near-infrared spectrum [31-32]. The extensive transparency range of 300 nm to 1100 nm establishes PACS as a very promising material for broadband optical communications, optical waveguides, and ultrafast photonic switching devices.

The optical band gap (Eg) of the PACS crystal was determined by Tauc's plot method, extrapolating the linear region of $(\alpha h\nu)^2$ versus photon energy (hν) to the energy axis, yielding a direct band gap of 1.8 eV. This band gap is moderately low, and therefore lower than that of typical semi-organic crystals. This suggests that copper incorporation has promoted strong electronic hybridization and enhanced intraband transitions [33]. Furthermore, the Urbach energy (E_u) was determined to be 0.41 eV, which suggests that a moderate level of structural disorder is advantageous for enhanced nonlinear optical (NLO) responses by allowing the formation of localized states within the band structure.

Further optical constants were investigated, and the extinction coefficient (k) was determined to be about 0.079, indicating substantial light absorption, especially in the UV region, which is useful for applications such as solar energy harvesting and NLO switching. The refractive index (n) of ~2.3 indicates excellent optical confinement and high polarizability in the material, which is crucial for effective light-matter interaction in photonic device topologies.

Table 5 shows the optical properties considered in material design objectives. The absorption edge at 281 nm, which increases overall optical transparency, is highlighted. PACS is a multidimensional material with a constant band gap of 1.8 eV, low Urbach energy, and a high refractive index, making it ideal for nonlinear optical modulators, photonic circuits, and optical energy devices.

PACS crystals are highly viable candidates for advanced optoelectronic, photonic, and energy-conversion applications, as evidenced by their integrated optical behavior, which encompasses a sharp absorption onset, a wide transparency window, a tunable band gap, and strong refractive and absorptive abilities.

3.4. Investigation of mechanical strength and resistance to plastic deformation in PACS crystals via vickers microhardness testing

The mechanical properties of Picolinic Acid Copper Sulfate (PACS) crystals were investigated to better understand their resistance to plastic deformation, which is an essential feature of materials utilized in nonlinear optical (NLO) devices, as shown in Figure 5 and 6. In many applications, the surface integrity of the material under strain has a direct impact on the device's performance. Therefore, it is imperative to maintain this integrity [34]. The purpose of this work is to determine the mechanical hardness of PACS crystals under various applied pressures, utilizing Vickers microhardness tests to get new insights into the material's behavior as shown in Table 6-8.

Table 6. Mechanical properties of PACS crystal under different loads.

Property	**25g**	**50g**	**100g**	**Description**
Indentation Diagonal (d) [mm]	0.101	0.095	0.087	The diagonal length of the indentation made by the indenter under different loads.
Vickers Hardness Number (Hv) [kg/mm^2]	45	65	95	The hardness of the material, calculated from the load and indentation size.
Vickers Hardness (Hv) [MPa]	441.32	637.46	931.67	The hardness in megapascals, derived from the Vickers hardness number.
Assumed Crack Length (c) [mm]	0.252	0.238	0.217	The assumed crack length based on indentation size, calculated as c ≈ 2.5d.
Assumed Young's Modulus (E) [MPa]	484.97	700.51	1023.81	The Young's modulus calculated from the Vickers hardness, assuming a Poisson's ratio of 0.3.
Elastic Recovery Ratio (E/Hv)	20.39	14.12	9.66	Ratio of Young's modulus to hardness, indicating material's elastic recovery.
Fracture Toughness ($K_{I}c$) [MPa·$m^{0.5}$]	0.14	0.25	0.48	The material's resistance to crack propagation, calculated from the crack length and hardness
Estimated Yield Strength (σ_Y) [MPa]	147.1	212.5	310.6	The estimated yield strength based on Vickers hardness and material properties.

Table 7. Parameter-wise view: Effect of log P on transport properties.

Parameter	Log P = 1.3	Log P = 1.6	Log P = 2.0	Description
P	19.9526	39.8107	100.0000	Parameter scaled with Log P; represents hydrophobicity strength
Log D (Predicted)	1.0532	1.1943	1.3824	Logarithmic form of predicted diffusion coefficient
D (Calculated)	11.3043	15.6432	24.1231	Actual diffusion rate (derived from Log D); indicates molecular mobility
Permeability Coeff. P_m (cm/s)	225,550.2139	622,765.1829	2,412,306.2000	Molecular permeability across membranes; increases with hydrophobicity
RTI (unitless)	0.7518	2.0759	8.0410	Retention Time Index; indicates how long the compound is retained in the system

Table 8. Comparative analysis of etched crystal surface morphologies (Images a–d) based on pit density, shape, and etching conditions.

Property	Figure 7 (a)	Figure 7 (b)	Figure 7 (c)	Figure 7 (d)
Observed Morphology	Well-defined striations or parallel grooves indicating anisotropic etching	Smooth surface with faint, blurry features	Moderate etching with visible lines; random orientation	Curved, irregular trench-like features
Relative Etch Pit Density	High	Very Low	Medium	Low to Medium
Pit Shape & Size	Large, elongated pits	Very small or no visible pits	Medium-sized, less uniform pits	Deep, non-uniform pits
Crystal Surface Behavior	Preferential orientation, possibly {100} plane with defects	Uniform/passivated surface; possibly isotropic etching	Mixed planes or defect-driven etching	High-defect region or grain boundary etching
Likely Etching Rate	High	Low	Moderate	Variable (localized high)
Possible Influencing Factors	High concentration or high temp; low pH	Low concentration or neutral pH; low temperature	Medium pH, moderate temp; presence of dislocations	Stress/strain effects or impurities

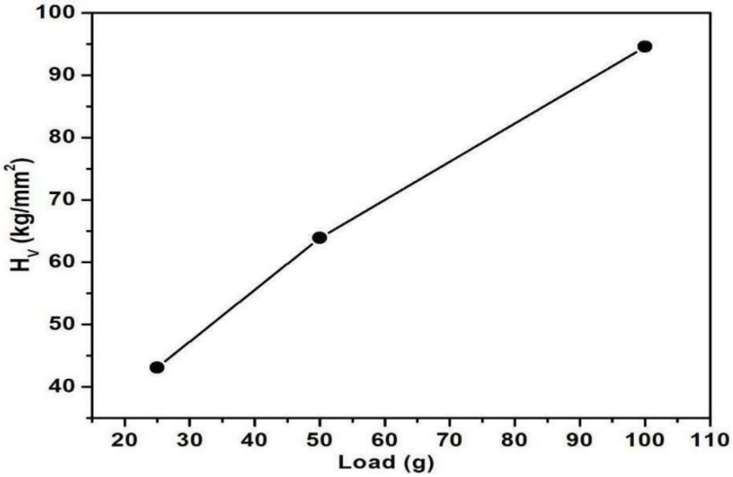

Figure 5. Load Vs Hardness.

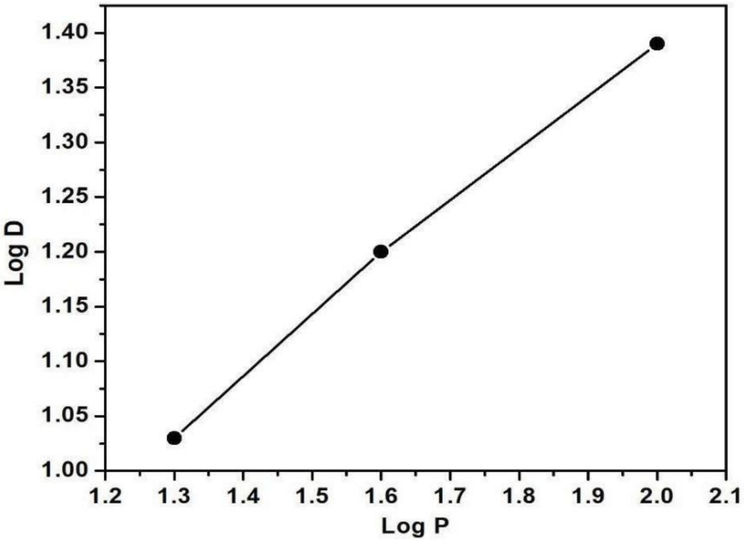

Figure 6. Log P Vs Log D.

3.4.1. Experimental setup

Microhardness measurements were obtained at room temperature using a Leitz Wetzler Vickers hardness tester, which guaranteed a smooth and level surface for consistent results. Different weights, ranging from 25 g to 100 g, were used to induce depression on the crystal's surface. To provide consistent and repeatable results, each load's indentation time was set to 15 seconds.

The Vickers Hardness Number (VHN) was calculated using the standard formula [35]:

$$W_{in} = \frac{1.8544 \times P}{d^2} \tag{2}$$

The Vickers hardness number (VHN) is calculated using a formula that incorporates the applied load and the geometry of the indentation. In this equation, **P** represents the applied load measured in kilograms, while **d** denotes the average length of the diagonal of the indentation in millimeters. The constant 1.8544 is a geometric factor that accounts for the specific shape of the diamond pyramid-shaped indenter used in the Vickers hardness test. This constant ensures that the hardness value accurately reflects the material's resistance to deformation under the applied load

Figure 5 shows the relationship between applied load and appropriate hardness levels. As expected, hardness increased with load up to 100 g, exhibiting typical load-dependent behavior in both elastic and plastic deformation regimes. This increase in hardness is caused by work hardening, which occurs when dislocations form and strengthen the crystal structure under stress. Beyond 100 g, surface cracking and multiple fractures appeared, indicating that the material had reached its mechanical limits. These microfractures are believed to result from the release of intrinsic internal stresses accumulated during crystal growth, which become more pronounced under mechanical strain.

3.4.2. Mayer's law and strain hardening behavior

Further examination of the mechanical characteristics of the PACS crystals was carried out by graphing the logarithmic applied load (log P) against the logarithmic diagonal length (log d), as shown in Figure 6. The experimental data were discovered to obey Mayer's law, which is stated as [36]:

$$P = k\,d^{n} \tag{3}$$

where P is the applied load, d is the diagonal length of the indentation, n is the Mayer's index or strain-hardening coefficient, and k is a material-specific constant. Taking the logarithm of both sides of Equation (5) yields [37]:

$$\text{Log } P = \log k + n \log d \tag{4}$$

Here, *P* represents the applied load, *d* denotes the diagonal length of the indentation, *n* is the Mayer's index or strain-hardening coefficient, and *k* is a material constant specific to the sample.

The slope of the log-log plot yields the value of *n*, which was discovered to be greater than 2 in PACS crystals, suggesting soft materials. Onitsch and Hanneman's classification classifies materials as hard ($n < 1.6$) or soft ($n > 1.6$). As a result, PACS crystals are categorized as soft materials, which explains the observed surface breakdown at higher stress levels.

3.4.3. Mechanical properties overview

The Vickers microhardness testing of PACS crystals yielded essential insights into their deformation characteristics and mechanical strength. The material exhibited significant work hardening up to 100 g; nevertheless, surface fractures at higher loads indicate a limitation in its mechanical strength. These discoveries are crucial for understanding the material's stability under stress, especially in device construction. Table 6 illustrates the mechanical characteristics of PACS crystals at various stress conditions.

3.4.4. Transport properties analysis

Further analysis of the material's transport properties was performed by examining the effect of the applied load on key transport parameters, as shown in Table 7. The relationship between the logarithmic applied load and transport properties such as hydrophobicity strength, diffusion coefficient, permeability, and retention time index is outlined. This data offers a broader understanding of how mechanical properties influence material transport characteristics under different conditions [38].

The Vickers microhardness testing of PACS crystals has yielded a thorough comprehension of the material's mechanical characteristics, encompassing its resistance to plastic deformation and load-bearing capability. The studies indicate that PACS crystals are comparatively soft materials, exhibiting increased hardness under stress until surface fracturing transpires. The impact of mechanical stress on transport parameters such as diffusion and permeability emphasizes the importance of these properties in device applications. The findings have a significant impact on the design of PACS-based systems, particularly in nonlinear optical applications that require stress resilience and surface integrity.

3.5. Etch-revealed surface morphology and growth mechanism of picolinic acid copper sulphate (PACS) crystals: A reflection microscopy study

Chemical etching is an efficient technique for assessing surface morphology and structural imperfections in single crystals. This research employed high-purity Millipore Water (resistivity 18.2 MΩ) as a gentle, non-destructive etchant to evaluate the surface quality of Picolinic Acid Copper Sulphate (PACS) crystals [39]. This choice ensured minimal contamination while still providing sufficient etching action to highlight surface and subsurface features without introducing artifacts. Well-grown, polished PACS crystal samples were subjected to immersion in the etchant for 10, 15, 20, and 25 seconds, respectively. After each interval, samples were rinsed and gently dried to preserve the native etched topography.

The etched surfaces were observed using an optical microscope in reflection mode at room temperature. The obtained micrographs revealed varied surface responses depending on etching duration and underlying microstructural characteristics [40]. Figure 7 shows an etched surface distinguished by elongated etch pits and step-like features. The linear striations indicate a two-dimensional, layer-by-layer growth pattern and suggest that etching occurred preferentially along specific crystallographic planes.

Table 8 contains a detailed analysis of the data, including a comparison of etched surfaces across many Figure 7 (a-d). The apparent striations and substantial etch pits in Figure 7 (a) depict anisotropic etching. The pits are likely related to defect-aligned orientation, such as the (100) plane. Image (b) shows a homogeneous design with a smooth surface and negligible pit development. The texture is influenced by the characteristics of passivated or isotropic etching performed under low-reactivity conditions. In contrast to the preceding Figure 7 (a) shows a major pit expansion. Figure 7 (c), which includes the image, shows considerable etching. Lines arranged in an arbitrary orientation and pits of a similar size distinguish this type of engraving. The etching was most likely created by a combination of plane and dislocation positions. The explanation is exceedingly persuasive. Figure 7 (d) shows that the material has these qualities because it has many flaws, as well as grain boundary etching and strain-induced reactivity. Each of these formations stands out for its irregular profundity and trench-like appearance.

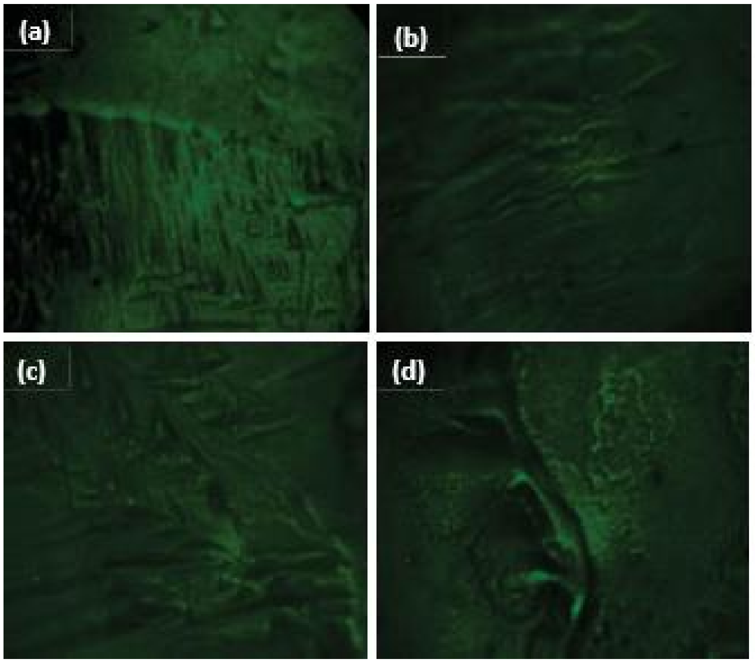

Figure 7. Etch pit pattern of PACS crystals for (a) 10 s (b) 15 s (c) 20 s (d) 25 s.

Table 9 shows how the reported morphologies are affected by etching concentration, pH, temperature, crystal orientation, and surface quality. It also shows how these results are related to process factors. For instance, Figure 7 (a)'s aggressive pit creation was most likely a result of high etching concentration and temperature, whereas Figure 7 (b)'s passivation may have been a result of low temperature and an almost neutral pH. In Figure 7 (c) and (d), you can see transitional etch patterns that could be areas of dislocation-driven kinetics, impurity incorporation, or mechanical strain. Low dislocation density and great structural homogeneity in the PACS crystal are inferred from the limited change in etch pattern across time intervals and the growing pit size.

Table 9. Parameters influencing etch morphology and their relative impact on images (a–d).

Parameter	Relative Impact on Observed Images (Figure 7)
Etching Concentration	Likely higher in (a), moderate in (c), lower in (b), localized in (d)
pH Level	Acidic in (a), closer to neutral in (b), moderate in (c, d)
Temperature	Likely high in (a), low in (b), moderate in (c, d)
Crystal Orientation	Anisotropic in (a), isotropic or passivated in (b), mixed in (c), boundary/interface in (d)
Surface Quality / Defects	Dislocation-driven in (c), (d); uniform in (b), defect-aligned in (a)
Time Effect	(a) may be initial or aggressive etch; (b) may be late stage or passivated; (c, d) show transitional features
Environmental Influence	Likely minimal here; (d) might indicate external stress/moisture impact

Table 10. Mean zone of inhibition for antibacterial activity of PACS crystal against bacterial pathogenic organisms (mm).

SAMPLE	ETHANOL Extract 100 μl added and Zone of inhibition (mm/ml)					Description of Antibacterial Activity
	25 μl	50 μl	75 μl	100 μl	Gentamicin antibiotic disc control	
Staphyloco-ccus aureus	14	18	22	26	20	Moderate activity; increases with concentration and surpasses control at 100 μl.
Staphyloco-ccus epidermidis	18	21	25	32	18	Strong activity; significantly exceeds control, especially at 100 μl.
E.coli	12	15	18	20	18	Mild to moderate activity: slightly higher than control at 100 μl.
Vibrio cholera	16	19	23	28	24	Strong response; consistent dose-dependent increase exceeding control.

The surface study, therefore, demonstrates the applicability of PACS crystals for applications where growth control and surface perfection are crucial, confirming a growth process that is primarily layer-type with localized structural variation.

3.6. Antimicrobial studies

The ability of Picolinic Acid Copper Sulphate (PACS) single crystals to kill bacteria was tested using the agar well diffusion method, which is a common way to find out how well bioactive substances kill bacteria in genetic studies as shown in Figure 8 and 9. This study aimed to assess the PACS crystal's inhibitory action against both Gram-positive and Gram-negative bacterial strains, highlighting its potential applications in medical and bio-optical device technologies.

(a)Staphylococcus aureus *(b) Staphylococcus epidermis*

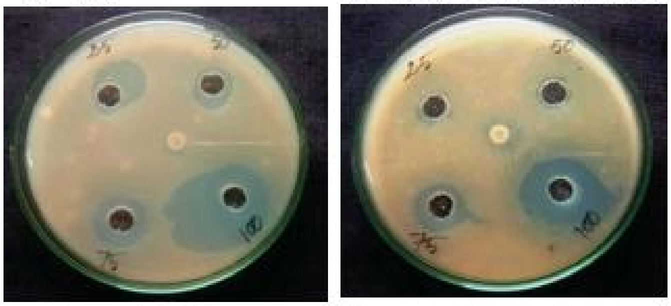

(c) E.coli *(d) Vibrio cholera*

Figure 8. Antibacterial activity of PACS crystal.

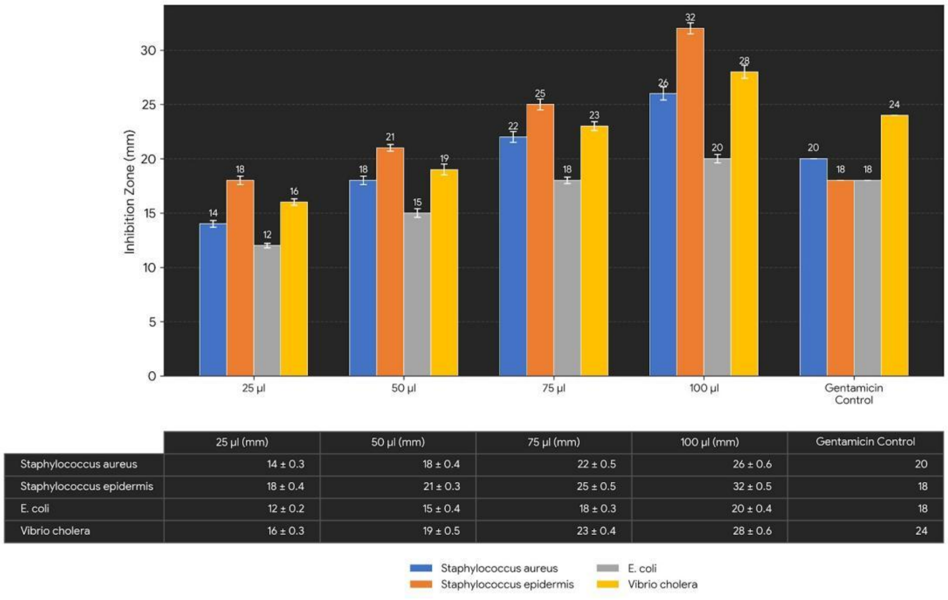

	25 µl (mm)	50 µl (mm)	75 µl (mm)	100 µl (mm)	Gentamicin Control
Staphylococcus aureus	14 ± 0.3	18 ± 0.4	22 ± 0.5	26 ± 0.6	20
Staphylococcus epidermis	18 ± 0.4	21 ± 0.3	25 ± 0.5	32 ± 0.5	18
E. coli	12 ± 0.2	15 ± 0.4	18 ± 0.3	20 ± 0.4	18
Vibrio cholera	16 ± 0.3	19 ± 0.5	23 ± 0.4	28 ± 0.6	24

Figure 9. Bar diagram for antibiotic variation of PACS crystal.

3.6.1. Bacterial strains and culture conditions

Four potentially pathogenic bacterial strains, encompassing both Gram-negative and Gram-positive bacteria, were selected for the antibacterial investigation. Gram-negative species included Vibrio cholerae and Escherichia coli, while Gram-positive bacteria encompassed Staphylococcus aureus and Staphylococcus epidermidis [41].

These bacteria are distinguished for their involvement in severe diseases and comprise a combination of both Gram classifications, providing a comprehensive overview of PACS's antimicrobial spectrum. The experimental bacteria were clinically isolated and stored in a laboratory environment. The growing substrate was nutrient agar medium. Approximately 25 milliliters of sterilized, molten nutritional agar were placed in pre-sterilized Petri plates and allowed to cool aseptically. Bacterial suspensions were prepared by dispersing the test bacteria in sterile distilled water and swabbing the surface of solidified agar with sterile cotton swabs to create a uniform bacterial lawn.

3.6.2. Well diffusion and sample application

The bacterial inoculum was evenly distributed on the agar surface, and 6 mm diameter wells were carefully cut with a flamed cork borer. Each plate had three wells for comparative analysis. The first well was filled with 50% PACS extract, while the second well contained 100% [42]. The third well, which served as a negative control, was filled with just the solvent used to dissolve the crystal extract in order to assess the solvent's baseline antibacterial efficacy. This approach allowed for a direct evaluation of PACS's antibacterial activity at two concentration levels while also ensuring that any observed inhibition was attributable to the PACS chemical rather than the solvent medium.

3.6.3. Incubation and observation

The infected Petri plates were incubated at 37°C for 24 hours to promote bacterial growth and enable the PACS chemical to permeate through the agar and interact with the bacteria. Following the incubation time, the zones of inhibition—clear patches surrounding the wells that hindered bacterial growth—were measured in millimeters using a calibrated ruler. These zones show the antibacterial activity of the PACS crystal extract.

3.6.4 Results and interpretation

Table 2 summarizes the antibacterial test results, and Figure 8 displays the zones of inhibition detected on the agar plates. The PACS crystal had significant antibacterial activity against all four bacterial strains tested. The level of inhibition varied with PACS concentration, with the 100% extract showing larger inhibition zones than the 50% extract, demonstrating dose-dependent antibacterial action [43].

Staphylococcus epidermidis, a Gram-positive bacterium, exhibited the largest zone of inhibition among the four types of microorganisms examined. This indicates that PACS is particularly effective at eliminating bacteria such as this one. The combination of picolinic acid and copper ions may enhance antibacterial effectiveness. Copper ions are known for their antibacterial properties, but picolinic acid can bond with metal ions, allowing it to maintain its biological effects [44]. These chemicals are thought to cause oxidative stress in bacterial cells, interfering with protein activity and damaging the cell wall. This comprehensive therapy method appears to be effective in eradicating S. epidermidis.

In addition to qualitative observations of inhibitory zones, PACS crystals' antibacterial activity was quantified to determine their potential as an antibacterial scaffold. The sizes of inhibition zones for four clinically relevant bacterial strains were determined using the agar well diffusion method, and they ranged from 12 mm to 32 mm, showing broad-spectrum antibacterial activity. The differences in inhibition zone sizes reflect varying sensitivities among bacterial species, which may be due to structural differences in Gram-positive and Gram-negative cell walls, the distinct mechanisms of action of copper ions and picolinic acid in disrupting cellular processes, and the permeability of bacterial membranes, which influences the diffusion and uptake of active compounds. To simplify comparative study, these inhibitory zone values were depicted as a bar diagram (Figure 9), clearly displaying the relative antibacterial activity of PACS crystals against each tested bacterium.

3.7. Third order NLO studies

The nonlinear optical properties of PACS (Picoli) have been investigated using the Z-scan technique, which has been implemented with both open and closed apertures as shown in Fig.10. This method is highly effective in measuring a number of critical third-order nonlinear optical properties, such as the nonlinear refractive index (n_2), nonlinear absorption coefficient (β), and the third-order nonlinear optical susceptibility ($\chi^{(3)}$). The results corroborate that PACS crystals possess significant third-order nonlinear optical characteristics, rendering them viable candidates for a diverse array of nonlinear optical applications, including optical switching, optical limiting, and optical modulation. The following section delves into the methodology, calculations, and importance of the results that were obtained.

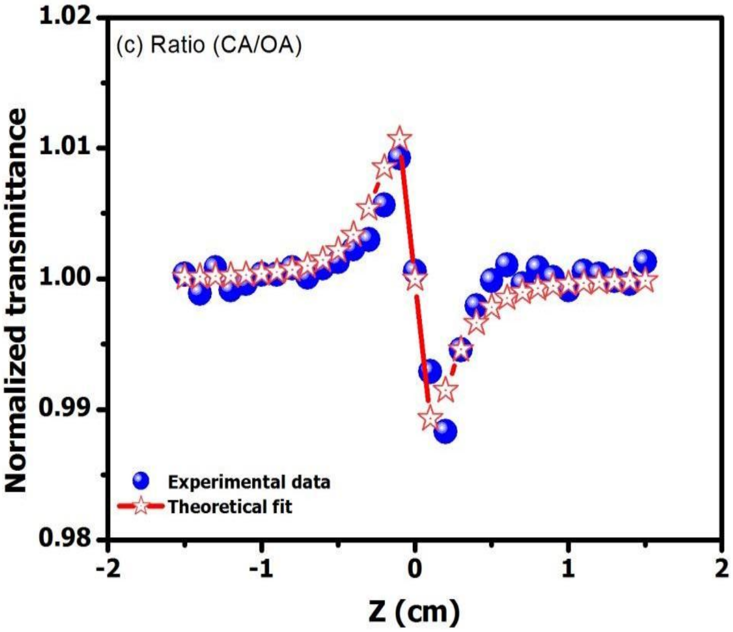

Figure 10. Open and closed aperture.

3.7.1. Transmittance difference (ΔTp-v)

The transmittance difference is used to analyze the closed-aperture Z-scan data. This information takes into consideration both the material's nonlinear refractive index and its absorption properties. The transmittance differential (ΔT_{p-v}) is dependent on both the aperture's linear transmittance (S) and the focal point's on-axis nonlinear phase shift ($\Delta\Phi_0$).

Used for analyzing closed-aperture Z-scan data [45]:

$$\Delta \mathrm{T}_{\mathrm{p-v}} = 0.406(1 - S)^{0.25}|\Delta\phi_o| \tag{5}$$

Here, *S* represents the aperture linear transmittance, and $\Delta\Phi_0$ denotes the on-axis nonlinear phase shift at the focal point

3.7.2 Aperture transmittance (S)

Aperture transmittance plays a crucial role in characterizing the nonlinear response of the material. With the aperture radius (r_a) set to 1.5 mm and the beam radius at the aperture (w_a) at 3 mm, the calculation allows us to quantify the material's ability to transmit light through the aperture while considering nonlinear interactions at different optical intensities.

Used for analyzing closed-aperture Transmittance Z-scan data [46]:

$$S = 1 - exp\left[-\left(\frac{\sqrt{2}r_a}{w_a}\right)^2\right] \tag{6}$$

In this setup, r_a denotes the radius of the aperture (1.5 mm), while w_a represents the radius of the laser beam at the aperture (3 mm).

3.7.3 Nonlinear refractive index (n_2)

The nonlinear refractive index (n_2) reflects the intensity-dependent refractive change in the material. This is derived from the Z-scan measurements [47], where:

$$n_2 = \frac{|\Delta \Phi_0|}{kI_oL_{eff}} \tag{7}$$

The nonlinear refractive index (n_2) reflects the intensity-dependent refractive change in the material, which is derived from Z-scan measurements. The wave number (k) is defined as $2\pi/\lambda$, where λ is the wavelength of the light. The intensity at the focus (I_0) is given as 0.01478 MW/cm^2. Additionally, L_{eff} represents the effective length of the material. Using these parameters, the nonlinear refractive index (n_2) of PACS crystals was calculated to be 3.51×10^{-10}cm^2/W, indicating strong intensity-dependent refractive effects, which are vital for optical switching and modulation applications.

$$L_{eff} = \text{Effective length} = \frac{1-\exp(-\alpha L)}{\alpha} \tag{8}$$

From these measurements, the nonlinear refractive index (n_2) of PACS crystals was found to be 3.51×10^{-10} cm^2/W, indicating strong intensity-dependent refraction, which is critical for optical switching and modulation applications.

3.7.4 Nonlinear absorption coefficient (β)

The nonlinear absorption coefficient (β) determines the material's ability to absorb light under high-intensity conditions. This is extracted from the open-aperture Z-scan measurements. The value of β for PACS crystals is calculated to be 3.81×10^{-6} cm/W, confirming significant nonlinear absorption processes, which is vital for optical limiting and protective applications.

ΔT is the normalized transmittance difference from the open aperture Z-scan.

$$\beta = \frac{2\sqrt{2}\Delta T}{I_oL_{eff}} \tag{9}$$

where I_0 is the on-axis laser intensity at the focal point, L_{eff} is the sample's effective interaction length, and ΔT is the difference between the peak and valley normalized transmittance derived from the open-aperture Z-scan curve.

Table 11. Z-Scan values for PACS crystals.

S.NO	Z-Scan Parameters	Z-Scan Values	Novelty Information
1	Laser power	100(mW)	Power density threshold for significant nonlinear effects
2	Laser wavelength	532 (nm)	Tuned for green laser applications, optimal for nonlinear studies
3	Focal length of the lens used	130 (mm)	Suitable focal length for minimizing beam divergence in Z-scan setup
4	Radius of aperture used	1.5 (mm)	Allows optimal light capture without introducing spatial distortions
5	Radius of the beam on the aperture	3 (mm)	Ensures uniform intensity distribution across the beam
6	Intensity of the laser at the focus	1.48×10^{7} (W/cm^{2})	Demonstrates moderate intensity for nonlinear optical effects
7	Rayleigh range (Z_R)	1.271 (mm)	Essential for measuring focal intensity and nonlinear behavior
8	Linear refractive index from Refractometer	1.6585	High refractive index supports significant nonlinear interaction
9	Nonlinear refractive index (n_2)	3.51×10^{-10} (cm^{2}/W)	Demonstrates strong nonlinear refraction suitable for optical switching
10	Nonlinear absorption coefficient (β)	3.81×10^{-6} (cm/W)	Critical for light absorption control in optical limiting applications
11	Real part of third-order nonlinear susceptibility (Re $\chi^{(3)}$)	2.44×10^{-8}(esu)	Indicates strong optical nonlinearity, beneficial for high-speed optical devices
12	Imaginary part of third-order nonlinear susceptibility ($\chi^{(3)}$)	4.09×10^{-8} (esu)	Enhances understanding of material's optical loss and absorption characteristicsc
13	Third-order nonlinear susceptibility ($\chi^{(3)}$)	4.77×10^{-8} (esu)	Comparable to high-performance optical materials in photonic devices
14	Beam Waist (w_0) [μm]	14.67 μm	Small beam waist promotes intense localized fields for nonlinear interactions
15	Peak Intensity (I_{peak}) [MW/cm²]	1.48×10^{12} MW/cm²	Indicates high peak intensity, essential for nonlinear optical effects
16	Absorption Length (L_a) [cm]	2.62×10^{5} cm	Represents the material's ability to absorb light over a large distance
17	Nonlinear Refraction Length (L_{n2}) [cm]	19.26 cm	Shows the length scale over which nonlinear refractive effects are significant
18	Spot Size at Focus (w_{focus}) [μm]	3001.11 μm	Large spot size ensures broad interaction area for nonlinear phenomena
19	$\chi^{(3)}$ from n_2 [cm²/W]	7.79×10^{3}cm²/W	Derived third-order susceptibility from nonlinear refractive index
20	$\chi^{(3)}$ from β [cm²/W]	1.61×10^{-13}cm²/W	Derived third-order susceptibility from nonlinear absorption coefficient

4. Third-order nonlinear optical susceptibility

Aperture transmittance is essential for identifying the nonlinear properties of the material. Setting the aperture radius (r_a) to 1.5 mm and the beam radius (w_a) to 3 mm facilitates the assessment of the material's ability to transmit light through the aperture, including nonlinear interactions at different optical intensities. A very important factor that controls how a material reacts to strong electromagnetic fields and how it bends and absorbs light is called third-order nonlinear optical susceptibility ($\chi^{(3)}$). This complex variable has a real component (Re $\chi^{(3)}$) that indicates its influence on the nonlinear refractive index and an imaginary component (Im $\chi^{(3)}$) that denotes its effect on nonlinear absorption. This study looked into the third-order nonlinear optical properties of PACS crystals in great detail. It used the Z-scan method and a continuous wave (CW) laser with a power of 100 mW and a wavelength of 532 nm.

The PACS crystal's nonlinear refractive index (n_2) was found to be 3.51×10^{-10} cm²/W, and its nonlinear absorption coefficient (β) was found to be 3.81×10^{-6} cm/W. The linear refractive index, measured using a refractometer, was 1.6585, and the Rayleigh range (Z_R) was calculated to be 1.271 mm. These results indicate a robust third-order nonlinear response. Found that the real and imaginary parts of $\chi^{(3)}$ are Re $\chi^{(3)} = 2.44 \times 10^{-9}$ cm²/W and Im $\chi^{(3)} = 4.09 \times 10^{-11}$ cm/W, which means that there is a lot of nonlinear refraction and a lot of nonlinear absorption. These findings demonstrate the potential for this material to be used in applications requiring strong nonlinear optical properties. This material shows promise for applications in optical switching and signal processing.

The magnitude of the total third-order susceptibility is given by the following relation [48]:

$$\left|\chi^{(3)}\right| = \sqrt{[Re(\chi^{(3)})]^2 + [Im(\chi^{3})]^2} \tag{10}$$

The calculation indicated that the value of $\chi^{(3)}$ is 4.77×10^{-8} esu, categorizing PACS crystals among materials with relatively high third-order nonlinear optical susceptibilities.

Table 11 summarizes the experimental conditions and corresponding Z-scan parameters for PACS crystals. Critical considerations include the laser power (100 mW), laser wavelength (532 nm), lens focal length (130 mm), and aperture radius (1.5 mm), all of which influence the reported nonlinear effects. Furthermore, the beam waist (14.67 μm), peak int4nsity (1.48×10^{12} MW/cm²), absorption length (2.62×10^{5} cm), nonlinear refraction length (19.26 cm), and focal spot size (3001.11 μm) provide further insights into the material's nonlinear optical characteristics. The data unequivocally indicate that PACS displays significant nonlinear refraction, as shown by the closed-aperture trace, and strong nonlinear absorption, as indicated in the open-aperture configuration. The elevated third-order susceptibility, around 10^{-8} esu, highlights the superior nonlinear optical characteristics of the material. These findings position PACS crystals as viable candidates for incorporation into sophisticated photonic and optoelectronic systems, especially for applications like optical switching, optical limiting, and all-optical signal processing.

4.1. Holistic analysis of structural and nonlinear optical properties of PACS crystals

The systematic studies on structural, optical, nonlinear optical, and antibacterial characteristics of PACS crystals prove their multifunctional use as a material, which is summarized in Table 12. The crystallinity analysis and structural stability were shown by the presence of a crystalline monoclinic structure with clear diffraction peaks as evidenced by the powder X-ray diffraction (PXRD) result. The raman spectroscopy showed the existence of specific vibrational modes and were associated with lattice and molecular vibrations, which once again confirms the framework of the PACS crystal. FTIR spectroscopy was used to determine that -OH, C=O, C-N, C-O and Cu-O vibrations are characteristic functional groups in the crystal lattice, which are used to confirm coordination of picolinic acid ligands and copper ions.

The optical analysis based on the UV-Vis spectroscopy showed a robust absorption in the ultraviolet region in which there was an optical band gap of about 1.8 eV, which was obtained after the Tauc plot assuming a direct allowed transition. This implies that the PACS material is a semiconducting optical material that can be used in optoelectronic. Well grown crystal surfaces had relatively uniform morphology and limited porosity, which is evidence of controlled crystal growth using Field Emission Scanning Electron Microscopy (FE-SEM).

Nonlinear optical properties studied by Z-scan technique The nonlinear optical characteristics of the investigated sample explored the nonlinear optical response property of the third-order nonlinear refractive index (n_2) of 3.51 x 10^{-10} cm^2/W, nonlinear absorption coefficient (b) of 3.81 x 10^{-6} cm/W, and third-order nonlinear optical susceptibility kh(3) of 4.77 x 10^{-8} esu which showed a strong nonlinear optical response characteristic of optical limiting and switching. The calculated absorption length ($\mathbf{L_a}\boldsymbol{b}$= 2.62 x 10^5 cm) and the nonlinear refraction length ($\mathbf{L_{n_2}}$ = 19.26 cm) are also another indication that PACS crystals have a great optical interaction ability.

Besides their optical ability, PACS crystals showed good antibacterial properties towards Gram-positive (Staphylococcus epidermidis and Staphylococcus aureus) and Gram-negative bacteria (Escherichia coli) with the inhibition zone of 14 mm to 32 mm based on the concentration. This antibacterial activity could probably be attributed to the availability of the Cu^{2+} ions in the crystal networks which are recognized to destabilize the bacterial cell walls and metabolism.

In general, the stable crystal structure, high nonlinear optical response, and good antibacterial activity of PACS crystals make them promising multifunctional materials of optoelectronic devices, optical limiting systems, and antimicrobial surfaces.

Table 12. Structural, compositional, and nonlinear optical characterization of PACS crystals.

Analysis	**PACS Crystals**
XRD (Structural & Lattice Analysis)	Crystalline monoclinic structure confirmed with well-defined diffraction peaks; nanocrystalline domains (~9.15 nm) indicating stable lattice framework
Raman (Bonding & Phonon Modes)	Distinct vibrational modes corresponding to ligand and lattice vibrations confirming structural integrity of the PACS framework
FTIR (Functional Groups & Metal–Ligand Interaction)	Characteristic vibrational bands of –OH, C=O, C–N, C–O, and Cu–O groups confirming coordination between picolinic acid ligands and Cu^{2+} ions
UV–Vis (Optical Absorption & Band Gap)	Strong absorption in UV region with an optical band gap of ~1.8 eV (Tauc plot), indicating semiconducting behavior suitable for optoelectronic applications
FE-SEM (Morphology & Microstructure)	Well-defined crystal surfaces with relatively uniform morphology and limited porosity, indicating controlled crystal growth

EDX (Elemental Composition)	Presence of Cu, S, O, N, and C confirming the expected stoichiometric composition of PACS crystals
XPS (Surface Chemical States)	Cu present in +2 oxidation state and sulfur as sulfate (SO_4^{2-}), confirming the chemical bonding environment in the PACS structure
Z-Scan (Nonlinear Optical Properties)	Significant third-order nonlinear optical response with $n_2 = 3.51 \times 10^{-10}$ cm^2/W, $\beta = 3.81 \times 10^{-6}$ cm/W, and $\chi(3) = 4.77 \times 10^{-8}$ esu, demonstrating strong nonlinear optical behavior
Antibacterial Activity	Effective antimicrobial activity against Gram-positive (S. aureus, S. epidermidis) and Gram-negative (E. coli) bacteria with inhibition zones of 14–32 mm
Optical Interaction Parameters	Absorption length ($L_a = 2.62 \times 10^5$ cm) and nonlinear refraction length ($L_{n_2} = 19.26$ cm) indicating strong optical interaction suitable for nonlinear photonic applications

Table 13. Summary of advanced PACS-based device models for multifunctional applications.

Application Concept	Functional Role of PACS	Design Insight	Potential Applications
PACS-Based Optical Modulator	Utilization of strong third-order nonlinear optical response for optical modulation	Integration of PACS crystals into optical waveguide platforms to enhance nonlinear interaction	Optical communication systems, photonic circuits, signal modulation
PACS-Antimicrobial Coating	Intrinsic antibacterial activity combined with structural stability	Embedding PACS crystals in polymer or ceramic matrices for durable antimicrobial coatings	Medical instruments, surgical tools, implant coatings
PACS-UV Photodetector concept	Semiconducting band gap (~1.8 eV) enabling photo-response under UV illumination	Hybrid structures combining PACS crystals with conductive electrodes for photoelectric detection	UV sensors, environmental monitoring, wearable device
PACS-Optical Limiter	Strong nonlinear absorption and nonlinear refractive index enabling optical limiting behavior	Use of PACS crystals as nonlinear optical elements for intensity -dependent attenuation	Laser safety systems, optical protection devices
PACS-Bio-Optical Sensor	Combination of optical activity and antibacterial properties for bio-detection platforms	Optical response changes used for monitoring biological or chemical interactions	Biosensors, pathogen detection, environmental diagnostics
PACS- Frequency Conversion Material	Nonlinear optical properties enabling frequency conversion processes	Integration in nonlinear optical devices for wavelength conversion	Spectroscopy systems, photonic instrumentation

5. Conclusion

The Picolinic acid copper sulfate (PACS) crystals were synthesized by slow evaporation method and systematically characterized to assess the structural, optical, nonlinear optical and antibacterial properties. Powder X-ray diffraction was used to establish that a well-crystalline monoclinic structure with good phase purity was formed. The characteristic functional groups and metal-ligand interactions in the crystal lattice were confirmed by Raman and FTIR spectroscopy. The optical analysis indicated a band gap of about 1.8 eV, which means the transparency of the material in the visible field is good, and it may be suitable in photonic work. The nonlinear optical properties were measured with Z-scan and yielded some degree of $n_2 = 3.51 \times 10^{-10}$ cm^2/W, b = 3.81 x 10^{-6} cm/W and $\chi^{(3)} = 4.77 \times 10^{-8}$ esu. The antibacterial tests showed effective inhibition with Staphylococcus aureus, Staphylococcus epidermidis and Escherichia coli. The performance of PACS crystals in optical and antibacterial tests provides a rationale to use the materials as future multifunctional materials in optical limiters and photonic devices, antimicrobial coatings, and optical limits.

Conflict of Interest: The authors declare that there is no conflict of interest regarding the publication of this paper.

Acknowledgments: The authors sincerely thank the management of Chennai Institute of Technology for providing the research infrastructure and support. We also acknowledge the PG and Research Departments of Physics at Thanthai Hans Rover College and National College for their technical assistance during the experimental analysis.

Funding: No specific funding was received from any public, commercial, or not-for-profit agencies for this research work.

Author Contributions

- **Raja Mohan O S**: Experimental design, crystal growth, and data collection.
- **M.S. Malar Selvi**: Spectroscopic characterization and validation.
- **R. Rathika**: Antibacterial studies and result interpretation.
- **Senthil S**: Project supervision, data analysis, manuscript writing, and correspondence.
- **T.U. Jeevitha**: Optical measurements and data processing.
- **J. Subashini**: Critical review, final editing, and technical guidance.

Data Availability: The data that support the findings of this study are available from the corresponding author upon reasonable request.

Declaration of Generative AI and AI-Assisted Technologies in the Writing Process: During the preparation of this work, the author(s) made limited use of ChatGPT (OpenAI) and similar AI-assisted tools solely for supportive purposes, such as verifying general information, suggesting structural clarity, and performing basic calculations. All core ideas, analysis, interpretations, and final content were developed and written by the author(s). The AI tools did not generate substantial sections of the text. The author(s) take full responsibility for the originality, accuracy, and integrity of the work.

References

1. Chandola, P.; Dwivedi, J.; Jamali, M.C. Non-linear optical activity and biological evaluation of organic compounds by experimental and theoretical techniques. *European Chemical Bulletin* 2023, 12(4), 19608–19619. https://doi.org/10.48047/ecb/2023.12.si4.1741.

2. Natarajan, R.; Meena, M.; Shalini, M.; Samuel Ebinezer, B.; Sundararajan, R.S.; Sabari Girisun, T.C. Growth and characterization of semi-organic, third-order nonlinear optical (NLO) phthalic acid potassium chloride (PAPC) single crystals. *Journal of Materials Science: Materials in Electronics* 2024, 35(25), 1692. https://doi.org/10.1007/s10854-024-13348-z.
3. Raja, R.; Sugaraj Samuel, R.; Hidayathullah, A.M.; Janarthanan, S. Synthesis, growth, optical, thermal, mechanical, and dielectric studies on nonlinear optical material: L-citrulline hydrochloride single crystals for photonic applications. *Journal of Materials Science: Materials in Electronics* 2023, 34(31), 2104. https://doi.org/10.1007/s10854-023-11539-8.
4. Slathia, G.; Singh, D.; Bamzai, K.K. Preparation, structural, spectroscopic, thermal, linear and nonlinear optical characteristics of semi-organic material: Samarium chloride–thiourea–L-tartaric acid. *Zeitschrift für Naturforschung A* 2019, 74(4), 339–352. https://doi.org/10.1515/zna-2018-0417.
5. Barry, D.E.; Caffrey, D.F.; Gunnlaugsson, T. Lanthanide-directed synthesis of luminescent self-assembly supramolecular structures and mechanically bonded systems from acyclic coordinating organic ligands. *Chemical Society Reviews* 2016, 45(11), 3244–3274. https://doi.org/10.1021/ic502384w.
6. Paździora, W.; Podolak, I.; Grudzińska, M.; Paśko, P.; Grabowska, K.; Galanty, A. Critical assessment of the anti-inflammatory potential of usnic acid and its derivatives—A review. *Life* 2023, 13(4), 1046. https://doi.org/10.3390/life13041046.
7. Mucha, P.; Skoczyńska, A.; Małecka, M.; Hikisz, P.; Budzisz, E. Overview of antioxidant and anti-inflammatory activities of selected plant compounds and their metal ion complexes. *Molecules* 2021, 26(16), 4886. https://doi.org/10.3390/molecules26164886.
8. Varshney, S.; Mishra, N. Pyridine-based polymers and derivatives: Synthesis and applications. In *Recent Developments in the Synthesis and Applications of Pyridines*. Elsevier, 2023; pp.43-69. https://doi.org/10.1016/B978-0-323-91221-1.00012-9.
9. Karim, I.; Munawar, K.S.; Abbas, S.M.; Karim, H.; Hussain, S.; Ashfaq, M.; Rehman, M. Synthesis, characterization, and photocatalytic degradation of nickel doped copper oxide nanoparticles. *Lahore Garrison University Journal of Life Sciences* 2020, *4*(2), 130-138.
10. Kargar, H.; Fallah-Mehrjardi, M.; Zare-Mehrjardi, H.R.; Dege, N.; Ashfaq, M.; Munawar, K.S.; Tahir, M.N. Copper(I) coordination polymers with bidentate Schiff base ligands: synthesis, spectral characterization, crystal structures, and electrochemical analysis. *Journal of the Iranian Chemical Society* 2026, 23, 18. https://doi.org/10.1007/s13738-025-03308-7.
11. Chen, X.; Wang, Y.; Zhang, L.; Li, J.; Zhao, H. (2025). Synthesis, crystal structure, and biological evaluation of a novel series of transition metal(II) complexes based on a Schiff base ligand. *Inorganic Chemistry Communications* 2025, 174, 115512. https://doi.org/10.1016/j.inoche.2025.115512.
12. Kargar, H.; Dege, N. A copper(II) chloride coordination compound with 2-phenyl-4,5-dihydro-1H-imidazole ligand: synthesis, characterization, crystal structure, HSA, and DFT studies.. *Journal of the Iranian Chemical Society* 2024, 21, 1561–1572. https://doi.org/10.1007/s13738-024-03016-8.
13. Kargar, H.; Fallah-Mehrjardi, M.; Dege, N.; Ashfaq, M.; Munawar, K.S.; Tahir, M.N.; Sahihi, M.; Bajgirani, M.A. Ultrasound irradiation synthesis of novel copper(II) complex with the 2-thiophenimidazoline ligand: SC-XRD, HSA, and DFT study. *Structural Chemistry* 2024, 35(5), 1437–1448. https://doi.org/10.1007/s11224-024-02295-4.
14. Chatterjee, A.K.; Chakraborty, R.; Basu, T. Mechanism of antibacterial activity of copper nanoparticles. *Nanotechnology* 2014, 25(13), 135101. https://doi.org/10.1088/0957-4484/25/13/135101.
15. Wang, L.; Hu, C.; Shao, L. The antimicrobial activity of nanoparticles: Present situation and prospects for the future. *International Journal of Nanomedicine* 2017, 12, 1227–1249. https://doi.org/10.2147/IJN.S121956.
16. Yancey-Gray, D.; Nyamwihura, R.; Arslan, Z.; Ogungbe, I.V. Antibacterial activities of copper, silver, and zinc-derived nanoparticles and their capacity to enhance the antimicrobial activities of antibiotics. *Current Nanoscience* 2025, 21(3), 423–456. https://doi.org/10.2174/0115734137301010240507101533.
17. Ge, R.; Sun, X.; Gu, Q.; Watt, R.M.; Tanner, J.A.; Wong, B.C.Y.; Xia, H.H.; Huang, J.-D.; He, Q.-Y.; Sun, H. A proteomic approach for the identification of bismuth-binding proteins in *Helicobacter pylori*. *JBIC Journal of Biological Inorganic Chemistry* 2007, 12(6), 831–842. https://doi.org/10.1007/s00775-007-0237-7.
18. Bhattacharyya, B.; Balischewski, C.; Pacholski, C.; Pandey, A.; Bald, I.; Taubert, A. Copper iron chalcogenide semiconductor nanocrystals in energy and optoelectronics applications—State of the art, challenges, and future potential. *Advanced Optical Materials* 2023, 11(8), 2202411. https://doi.org/10.1002/adom.202202411.

19. Luo, M.; Wei, C.; Wu, Y.; Lei, W.; Zhang, X.; Zeng, H. All-inorganic perovskite film photodetectors with tailored deposition techniques and component engineering. *Journal of Materials Chemistry C* 2024, 12(31), 11675–11711. https://doi.org/10.1039/D4TC02003K.
20. Mahmoudi, G.; Sahli, S.; Tamer, O.; Çınar, E.B.; Böhme, U.; Dege, N.; Ben Nasr, C.; Kaabi, K. Investigation on crystal structure, spectral FT-IR analysis, DFT and molecular docking studies of a novel complex with N′-(pyridin-2-ylmethylene)nicotinohydrazide. *Journal of Molecular Structure* 2022, 1269, 133741. https://doi.org/10.1016/j.molstruc.2022.133741.
21. Kim, H.-S.; Patel, M.; Kim, J.; Jeong, M.S. Growth of wafer-scale standing layers of WS_2 for self-biased high-speed UV–visible–NIR optoelectronic devices. *ACS Applied Materials & Interfaces* 2018, 10(4), 3964–3974. https://doi.org/10.1021/acsami.7b16397.
22. Sunagawa, I. Mechanism of crystal growth, etching and twin formation of hematite. *Mineralogical Journal* 1960, 3(2), 59–89. https://doi.org/10.2465/minerj1953.3.59.
23. Tsuchida, H.; Kamata, I.; Nagano, M. Investigation of defect formation in 4H-SiC epitaxial growth by X-ray topography and defect selective etching. *Journal of Crystal Growth* 2007, 306(2), 254–261. https://doi.org/10.1016/j.jcrysgro.2007.05.006.
24. Feng, X.; Ma, J.; Xu, K.; Wu, Y.; Zhai, Y.; Xuan, F.; Zhai, D.; Cao, L.; Teng, B. Design, growth, and characterization of novel Schiff base organic nonlinear optical crystals PAC and PAB. *Journal of Molecular Structure* 2025, 1327, 141200. https://doi.org/10.1016/j.molstruc.2024.141200.
25. Punz, B.; Christ, C.; Waldl, A.; Li, S.; Liu, Y.; Johnson, L.; Auer, V.; et al. Nano-scaled advanced materials for antimicrobial applications – mechanistic insight, functional performance measures, and potential towards sustainability and circularity. *Environmental Science: Nano* 2025, 12(3), 1710–1739. https://doi.org/10.1039/D4EN00798K.
26. Vediyappan, S.; Chaudhary, A.K.; Mottamchetty, V.; Arumugam, R.; Gandhiraj, V.; Pandian, M.S.; Perumalsamy, R. Evaluation of linear and nonlinear optical properties of D−π−A type 2-amino-5-nitropyridinium dihydrogen phosphate (2A5NPDP) single crystal grown by the modified Sankaranarayanan–Ramasamy (SR) method for terahertz generation. *Crystal Growth & Design* 2019, 19(12), 6873–6892. https://doi.org/10.1021/acs.cgd.9b00382.
27. Belik, A.A.; Iikubo, S.; Yokosawa, T.; Kodama, K.; Igawa, N.; Shamoto, S.; Azuma, M.; et al. Origin of the monoclinic-to-monoclinic phase transition and evidence for centrosymmetric structure of $BiMnO_3$. *Journal of the American Chemical Society* 2007, 129(4), 971–977. https://doi.org/10.1021/ja0664032.
28. Gao, P.-J.; Liu, J.-R. A Cu(II)-based coordination polymer: Catalytic properties and stroke treatment. *Designed Monomers and Polymers* 2022, 25(1), 148–154. https://doi.org/10.1080/15685551.2022.2086396.
29. Ghosh, N.; Bandyopadhyay, A.; Roy, S.; Saha, G.; Mondal, J.A. Unified view of the hydrogen-bond structure of water in the hydration shell of metal ions (Li+, Mg2+, La3+, Dy3+) as observed in the entire 100–3800 cm−1 regions. *Journal of Molecular Liquids* 2023, 389, 122927. https://doi.org/10.1016/j.molliq.2023.122927.
30. Lemmetyinen, H.; Tkachenko, N.V.; Valeur, B.; Hotta, J.; Ameloot, M.; Ernsting, N.P.; Gustavsson, T.; Boens, N. Time-resolved fluorescence methods (IUPAC Technical Report). *Pure and Applied Chemistry* 2014, 86(12), 1969–1998. https://doi.org/10.1515/pac-2013-0912.
31. Luo, Y.; Ruan, Z.; Guo, Z.; Chen, Y.; Lin, H.; Ge, M.; Zhu, C. Electron orbital hybridization–enhanced copper nanocatalysis for anti-infection. *Advanced Functional Materials* 2024, 34(22), 2313742. https://doi.org/10.1002/adfm.202313742.
32. Zhu, K.; Carignan, G.M.; Teat, S.J.; Rangan, S.; Hei, X.; Nguyen, L.H.; Li, J. Narrow band gap hybrid copper(I) iodides. *Chemistry of Materials* 2024, 36(22), 11139–11149. https://doi.org/10.1021/acs.chemmater.4c02044.
33. Harris, K.D.; Elias, A.L.; Chung, H.-J. Flexible electronics under strain: a review of mechanical characterization and durability enhancement strategies. *Journal of Materials Science* 2016, 51(6), 2771–2805. https://doi.org/10.1007/s10853-015-9643-3.
34. Ghorbal, G.B.; Tricoteaux, A.; Thuault, A.; Louis, G.; Chicot, D. Comparison of conventional Knoop and Vickers hardness of ceramic materials. *Journal of the European Ceramic Society* 2017, 37(6), 2531–2535. https://doi.org/10.1016/j.jeurceramsoc.2017.02.014.
35. Mayer, R. E. Structural analysis of science prose: Can we increase problem-solving performance? *ACM SIGDOC Asterisk Journal of Computer Documentation* 1995, 19(3), 3–25. https://doi.org/10.1145/216708.216709.

36. Xing, L.; Glen, R.C. Novel methods for prediction of logP, pKa, and logD. *Journal of Chemical Information and Computer Sciences* 2002, 42(4), 796–805. https://doi.org/10.1021/ci010315d
37. Gaskell, D.R.; Krane, M.J.M. *An introduction to transport phenomena in materials engineering*. CRC Press, 2024. https://doi.org/10.1201/9781003104278.
38. Goniszewski, S.; Adabi, M.; Shaforost, O.; Hanham, S.M.; Hao, L.; Klein, N. Correlation of p-doping in CVD graphene with substrate charges. *Scientific Reports* 2016, 6, 22858. https://doi.org/10.1038/srep22858.
39. Ramakrishnaiah, R.; Alkheraif, A.A.; Divakar, D.D.; Matinlinna, J.P.; Vallittu, P.K. The Effect of hydrofluoric acid etching duration on the surface micromorphology, roughness, and wettability of dental ceramics. *International Journal of Molecular Sciences* 2016, 17(6), 822. https://doi.org/10.3390/ijms17060822.
40. Tavares, T.D.; Antunes, J.C.; Padrão, J.; Ribeiro, A.I.; Zille, A.; Amorim, M.T.P.; Ferreira, F.; Felgueiras, H.P. Activity of specialized biomolecules against bacteria. *Antibiotics* 2020, *9*(6), 314. https://doi.org/10.3390/antibiotics9060314.
41. Al-Hujaily, E.M.; Mohamed, A.G.; Al-Sharif, I.; et al. PAC, a novel curcumin analogue, has anti-breast cancer properties with higher efficiency on ER-negative cells. *Breast Cancer Research and Treatment* 2011, 128, 97–107. https://doi.org/10.1007/s10549-010-1089-3.
42. Khan, M.F.; Tang, H.; Lyles, J.T.; Pineau, R.; Mashwani, Z.-U.-R.; Quave, C.L. Antibacterial properties of medicinal plants against MDR pathogens. *Frontiers in Pharmacology* 2018, 9, 815. https://doi.org/10.3389/fphar.2018.00815.
43. Božić Cvijan, B.; Jačić, J.K.; Bajčetić, M. Impact of copper ions on antibiotic activity. *Molecules* 2023, 28(13), 5133. https://doi.org/10.3390/molecules28135133.
44. Namarathne, D.L.; Walden, S.L.; Donaldson, R.E.; Jaatinen, E.A. Using image analysis to determine ideal aperture conditions for optimal Z-scan signal quality. *IEEE Journal of Quantum Electronics* 2018, 54(3), 1–9. https://doi.org/10.1109/JQE.2018.2829490.
45. Zheng, X.; Zhang, Y.; Chen, R.; Cheng, X.; Xu, Z.; Jiang, T. Z-scan measurement of nonlinear refractive index of monolayer WS_2. *Optics Express* 2015, 23(12), 15616–15623. https://doi.org/10.1364/OE.23.015616.
46. Sheik-Bahae, M.; Said, A.A.; Wei, T.H.; Hagan, D.J.; Van Stryland, E.W. Sensitive measurement of optical nonlinearities using a single beam. *IEEE Journal of Quantum Electronics* 1990, 26(4), 760–769. https://doi.org/10.1109/3.53394.
47. Sheik-Bahae, M.; Said, A.A.; Van Stryland, E.W. High-sensitivity, single-beam n_2 measurements. *Optics Letters* 1989, 14(17), 955–957. https://doi.org/10.1364/OL.14.000955.
48. Shen, Y. R. The Principles of Nonlinear Optics. *Wiley*, 1984. https://doi.org/10.1017/S0263034600001889.